Flow Field Interference Effect on Energy Harvesting Enhancement of a Combined Fluid-Structure Interaction System in Channel Flow

Physics of Fluids ARTICLE pubs.aip.org/aip/pof

Flow field interference effect on energy harvesting enhancement of a combined fluid–structure interaction system in channel flow

Cite as: Phys. Fluids **36**, 023606 (2024); doi: 10.1063/5.0185041
Submitted: 28 October 2023 · Accepted: 12 January 2024 ·
Published Online: 7 February 2024

Massoud Tatar[a] and Hua-Dong Yao (姚华栋)

AFFILIATIONS

Department of Mechanics and Maritime Sciences, Chalmers University of Technology, 412 96 Gothenburg, Sweden

[a]Author to whom correspondence should be addressed: massoudt@chalmers.se

ABSTRACT

In this paper, the flow field between two vibrating systems and the potential to increase the harvested energy by the interference of flow fields was numerically evaluated. A combined configuration of a cylinder-splitter hyperelastic plate placed at the wake of a vortex-induced oscillating cylinder was studied in a laminar channel flow at a Reynolds number of 200. A finite-volume method was adopted for solving the flow field over polyhedral cells. Overset grid and mesh morpher algorithms were employed to handle different mesh motions. On the other hand, a finite element method was exploited to solve the structural displacement of the hyperelastic plate. Having validated two individual similar systems, the effects of different spacing values and the reduced frequency of the vibrating cylinder on the amount of harvested energy were investigated in the combined configuration. According to results, no flow unsteadiness took place for the small spacing values at low reduced velocity. Increasing the natural frequency, the oscillation of the vibrating cylinder excited its boundary layer, causing it to separate. Moreover, the presence of such oscillations at downstream of the vibrating cylinder altered its response yielding higher energy production. Results showed that at some specific reduced velocities of the oscillating cylinder, the vortex shedding phenomenon did not occur if the spacing between the cylinders was small. However in other cases, the relative power efficiency of the oscillating cylinder in the combined system was increased from 29% to more than five times of the isolated oscillating cylinder depending on the parameters.

I. INTRODUCTION

Due to daily rise of energy demands and global concerns on climate change caused by fossil-based traditional ways of energy conversion, clean and renewable sources of energy generation have been greatly noticed. In the context of energy harvesting by mechanical systems from different dynamic systems including wind and water flows, several influential principles of modulations and parameters were reviewed in the literature.[1] A variety of flows were investigated by researchers to evaluate different mechanisms of extracting energy by flow-induced vibrations (FIV). There are four recognized types of physical phenomena in FIV including flutter, wake galloping, vortex-induced vibrations (VIV), and galloping. In a VIV problem, the maximum amplitude of harmonic oscillations is expected to take place while the frequency of vortex shedding behind the bluff body gets close to the natural frequency of structure eigenmode. A wide range of research work either experimentally or numerically conducted from FIV was reviewed in the literature.[2] It is known that for a one degree-of-freedom elastic cylinder, the maximum amplitude of oscillations can be obtained when the frequency of cylinder vortex shedding lies close to the natural frequency of structure and "lock-in" condition happens.[3–6] Results show synchronization occurs when the multiplication of structural mass-damping ratios is close to 0.25 over a range of reduced velocities.[7]

For a confined oscillating cylinder at low Reynolds laminar flow, it is also reported that the maximum extracted energy is possible when the mass-damping parameter, $m^*\zeta$, is close to 0.25–0.3.[8] To increase the amplitude of a VIV harvester over a broad range of flow speed, different shapes of bluff body were evaluated in the literature.[5,9–16] In the context of two tandem cylinders in an unconfined laminar flow, published results reveal that for a spacing distance of more than 4.5 times the cylinder diameter, the root mean square values of lift coefficient for both upstream and downstream cylinders increase significantly.[17] There are extensive reviews in this field describing the flow characteristics and lift/drag force variations in terms of flow Reynolds number and distance between tandem cylinders with or without the same shape or diameter and the effects of wake interference.[18–20]

From energy extraction perspective, it is reported that VIV of an elastic isolated cylinder in a confined laminar channel flow can increase the amount of peak power efficiency up to an order of magnitude greater than that of an unconfined case.[8] The hydrodynamic flow features of in-series bluff bodies with two different cross sections were numerically studied for circular-square cylinder system for various spacing and radius ratio in confined channel.[21,22] The effect of spacing and cross-section configuration are reported for different reduced velocities. On the other hand, a number of work is published on energy conversion by using piezoelectric harvesters (PEH) by either placing the PEH in the wake of a bluff body at some specific distances or attaching it to a bluff body as a splitter flexible plate generating electrical voltage from plate deformations in both laminar and turbulent flows.[11,23–29] The potential application of such small scale devices can be to supply energy for micro sensors which are working with chemical batteries.[30] Although extensive work was published on oscillating isolated or tandem cylinders as well as splitter flexible plate attached to bluff bodies for energy harvesting applications, to the best of authors' knowledge, no study has been established to investigate the flow field interaction between the tandem cylinders and a hyperelastic splitter plate in downstream to evaluate the flow interference and any possibility for improving the power efficiency generated by such combined systems. Thus, in this research, a combined configuration of tandem cylinders and a hyperelastic splitter plate confined in a channel are numerically studied using STAR-CCM+. The aim of this study is to investigate the two-way interaction between the shed vortices from one vibrating cylinder in front and one fixed cylinder-elastic plate system in rear locations and to explore if the interaction of such combined system could produce more energy than each individual system. The upstream cylinder is mounted on a spring-damper system and undergoes oscillations due to the VIV effect. The downstream cylinder, however, is kept stationary, and the attached splitter plate experiences elastic deformations. The distance between two cylinders as well as the reduced velocity of the upstream cylinder are changed, and the power efficiency extracted from the VIV cylinder and the tip displacement of the splitter plate are computed and discussed. To avoid high computational cost for fluid–structure interactions in three dimensional domain, a one-cell thickness approach is employed following the literature for a laminar flow.[31]

This paper is organized as follows: Sec. II describes the governing equations of both fluid and solid dynamics, the fluid–structure interaction, the mesh motion technique, and the power extraction formulations for both the oscillating cylinder and the piezoelectric plate. In Sec. III, validation of the numerical methods used in this study is reported on two different benchmark problems, i.e., a hyperelastic plate attached to a fixed cylinder in a channel flow and an oscillating vortex-induced low mass-ratio cylinder in farfield. Having assured on the reliability of the numerical methods for the hyperelastic plate deformation and the cylinder rigid body oscillation, the main problem is extensively studied. A schematic introduction of the combined case including of an oscillating low-mass ratio cylinder placed in the upstream of a stationary cylinder attached to a splitter flexible plate is presented in Sec. IV. The results of fluid–structure coupled simulations for different parameters of interest are given in Sec. V and compared to the isolated conditions. In the end, a summary and conclusion is expressed in Sec. VI.

II. NUMERICAL APPROACH

A. Fluid dynamics model

The Navier–Stokes governing equations for a laminar, incompressible Newtonian fluid flow on a moving domain are as follows:

$$\nabla \cdot \overrightarrow{u_f} = 0, \tag{1}$$

$$\rho_f \left(\frac{\partial \overrightarrow{u_f}}{\partial t} + \overrightarrow{u_f} \nabla \cdot \overrightarrow{u_f} \right) = -\overrightarrow{\nabla p} + \mu \nabla^2 \overrightarrow{u_f}, \tag{2}$$

where ρ_f and μ are the density and dynamic viscosity of the fluid, respectively, and $\overrightarrow{u_f}$ and p are the fluid velocity vector and pressure of the flow, respectively. The equations are discretized using the second-order accuracy in space and time using a finite volume approach. Polyhedral grids were adopted to discretize the CFD domain whose great advantage is more accurate approximation of gradients because of inclusion of more neighboring points.[32,33] Moreover, this type of grid is more robust to stretching than tetrahedral ones, thus making it more popular for predicting flows with separation and highly vortical patterns.

B. Structural dynamics model

To compute the deformation of the hyperelastic plate, the following momentum equation is numerically solved using a finite element approach:

$$\rho_s \frac{\partial^2 \overrightarrow{u_s}}{\partial t^2} = \nabla \cdot \boldsymbol{\sigma_s} + \rho_s \overrightarrow{f}, \tag{3}$$

where ρ_s is the hyperelastic plate density, $\overrightarrow{u_s}$ is the dislacement vector, $\boldsymbol{\sigma_s}$ is the Cauchy stress tensor, and $\overrightarrow{f}$ denotes any body force. Assuming a Saint Venant–Kirchhoff material, the constitutive equation can be recast using the second Piola–Kirchhoff stress tensor and the Green-Lagrange strain tensor.

To include the dynamics of the two-dimensional oscillating cylinder, it is modeled as a rigid body of mass m attached to a linear spring and viscous damper. The spring and damper constants are k_s and c, respectively. The cylinder has only transverse motion in the y direction. Thus, the governing equation is a second-order ordinary differential one, i.e.,

$$\ddot{y} + 2\zeta\omega_n\dot{y} + \omega_n^2 y = \frac{F_y}{m}, \tag{4}$$

where F_y is the flow force on the cylinder in the y direction, $\omega_n = \sqrt{k_s/m}$ is the angular frequency, and ζ is the damping coefficient, defined by

$$\zeta = \frac{c}{2\sqrt{k_s m}}. \tag{5}$$

C. Fluid–structure coupling

Similar to the procedure exploited and described in a recent two-way FSI work on hydroelastic analysis of slamming induced impact,[34] Fig. 1 demonstrates the fully coupled algorithm employed in this study to control the acceleration effects of the highly flexible plate on the solution stability. Having initialized the flow domain, the CFD solver updates the flow variables and interpolates the pressure values to the hyperelastic plate interface. Then, the FEM solver calculates the nodal

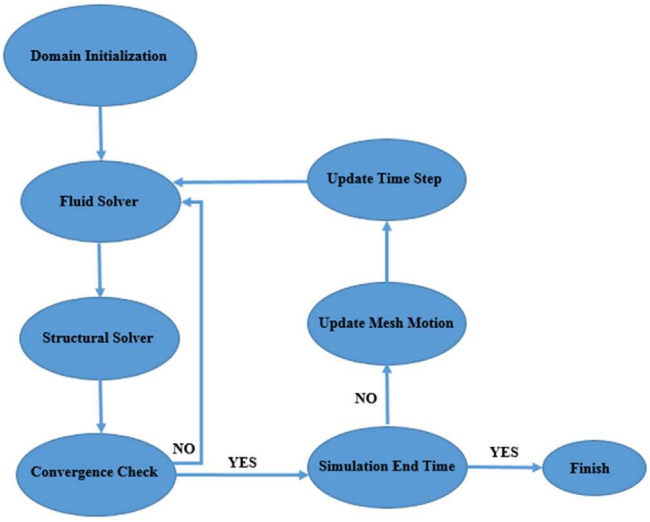

FIG. 1. Fully coupled FSI algorithm.

displacements. While the residuals are above a threshold or the minimum iterations are not reached, the fluid and structure solvers iterate simultaneously to obtain an equilibrium solution at each time step. Having met the prescribed convergence criteria, the node position in the flow domain is updated using the mesh morphing algorithm and the time advances. This procedure is continued until the outer stopping conditions are met.

D. Mesh motion

In order to handle large deformations of hyperelastic splitter plate as well as cylinder oscillatory motions due to the fluid flow, two different techniques were employed in this study. In the hyperelastic splitter plate, a mesh morphing method was selected. In this approach, a preconditioned conjugate gradient method and a fast multipole technique are applied to the typical radial basis functions used for displacement control points around the moving boundary. To include the displacement of oscillatory cylinder on the other hand, an overset grid motion was utilized which preserves the original mesh quality and is beneficial for rigid body displacement of the cylinder resulting from the net value of the fluid flow, spring and damper forces. In this case, the overset domain containing the oscillatory cylinder is being displaced at each time step based on the solution of Eq. (4).

E. Energy conversion and power extraction

The power harnessed by an oscillator from the flow kinetic energy through a period of motion, T_{osc} is computed as

$$P_{osc} = \frac{1}{T_{osc}} \int_0^{T_{osc}} F_y \dot{y} dt, \tag{6}$$

where $\dot{y}$ is the transverse velocity of the oscillator. Furthermore, the total kinetic energy of the flow passing over the oscillator with a unit length is given by

$$P_{tot} = \frac{1}{2} \rho U^3 D. \tag{7}$$

Therefore, the extracted power efficiency of the cylinder under VIV can be evaluated as

$$\eta_{VIV} = \frac{P_{osc}}{P_{tot}}. \tag{8}$$

Moving on to the dynamics of the elastic plate subjected to fluid motion, many studies have introduced two governing nondimensional parameters as follows:[35–37]

$$K_b = \frac{E_s}{12 \rho_f U^2} \left(\frac{h}{L}\right)^3, \tag{9}$$

$$M = \frac{\rho_s h}{\rho_f L}, \tag{10}$$

where Eq. (9) denotes the bending stiffness and Eq. (10) represents the mass ratio. In this context, the elastic plate fixed at one end is treated as an Euler–Bernoulli beam, and its natural frequency can be computed by the following equation:[38]

$$f_{ni} = \frac{k_i^2}{2\pi L} \sqrt{\frac{K_b}{M}}, \tag{11}$$

where $i = 1, 2, 3$ represents the mode numbers of plate and k_i are three constants, respectively. In this framework, the generated power of a piezoelectric plate as an inertial harvestor is identified to be proportional to the amplitude of tip displacement, y_t, as well as to the third power of response frequency, f, of a cantileverd piezo-beam

$$P_{piezo} \propto y_t \propto f^3. \tag{12}$$

III. METHODOLOGY VALIDATION

In this section, two benchmark cases were investigated and compared with references to ensure the correctness of numerical settings and considerations for the fluid–structure interaction treatment. The first one is a highly flexible flat plate attached to a fixed cylinder within a channel and exposed to the laminar flow, and the second one is a low mass-ratio oscillating cylinder subjected to freestream flow.

A. Isolated stationary cylinder-elastic plate in a laminar channel flow

Turek and Hron[39] extensively studied the effects of solid material properties as well as flow Reynolds number on the displacement behavior of a hyperelastic plate attached to a fixed cylinder in a laminar channel flow. The accurate capturing of vortex shedding and added mass effects of highly deforming plate and the proper grid motion in the presence of channel walls characterizes the problem as a challenging benchmark which has been widely simulated by the literature to validate different fluid–structure interaction schemes and numerical algorithms.[39–42] The computational domain is the same as Ref. 39. The Reynolds number is 200 based on the cylinder diameter. At inlet, a parabolic velocity profile was imposed. No-slip wall was set on lateral sides of channel, as well as cylinder and splitter plate faces and a pressure-outlet condition was considered for the exit boundary. To avoid any discontinuity at the fluid–structure interface, the following physical relations are met:

$$\begin{aligned} \overrightarrow{u_f} &= \dot{\overrightarrow{u}}_s, \\ \boldsymbol{\sigma}_f . \overrightarrow{n} &= \boldsymbol{\sigma}_s \cdot \overrightarrow{n}, \end{aligned} \tag{13}$$

TABLE I. Properties of the solid elastic material.

Parameters	$E_s/(\rho_f U^2)$	ρ_s/ρ_f	ν_s
Value	1400	1	0.4

where $\boldsymbol{\sigma}$ is stress tensor and $\vec{n}$ is the unit normal vector of the interface.

To avoid the occurrence of "shear-locking" in deformations with large bending, quadratic hexahedron elements were used to discretize the governing equations on the hyperelastic plate. In addition, the polyhedral grids were employed for discretization of the flow field to increase the accuracy of gradients of such highly vortical flows.[43] One-cell thickness approach was adopted in depth direction to reduce computational cost.[31] The first grid over the cylinder was placed at $10^{-3}D$, and the grid base size of $0.05D$ was selected for the fluid domain. Since only the pressure force acting on the hyperelastic plate was of interest, no boundary layer mesh was made on the plate surfaces. The solid domain was divided into 450 hexahedral grids. A normalized time step size of 0.02 was utilized for temporal integration of simulations where the flow timescale was computed based on the cylinder diameter and the mean inlet velocity. Normalized values of elasticity and density of the solid plate and the Poisson ratio used in this simulation are given in Table I.

Figure 2 shows the velocity contour of this benchmark problem. A low velocity region is formed near the no-slip channel walls interacting with the accelerated flow region generated by the favorable pressure gradient of the cylinder. This region is further affected by the plate deformation causing it to become elongated in the streamwise direction. The shed vortices are confined by walls of the channel and get merged soon after the plate tip, as seen here.

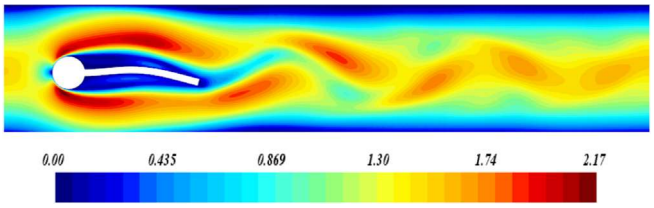

FIG. 2. Contour of normalized velocity magnitude, U/U_{ref}.

TABLE II. Grid independency analysis.

Grid size	Frequency (Hz)	Y_{tip}/D
Base	5.28	(0.016 ± 0.337)
Fine	5.29	(0.017 ± 0.341)

The vortex shedding from the cylinder makes the splitter plate vibrate with a frequency close to its natural mode in a vacuum condition. In Fig. 3, normalized tip displacement and lift coefficient of the plate obtained from the present simulation are compared with literature[39] demonstrating appropriate accordance in both amplitude and frequency values. The reference frequency and normalized tip displacement amplitude are 5.3 Hz and 0.0148 ± 0.343, respectively.

To ensure the independency of the plate deformation from grid and time step sizes, a resolution analysis was performed for both. In Table II, grid sensitivity results are reported where two different base sizes of $0.05D$ and $0.025D$ for fluid domain and two total solid cell numbers of 450 and 700 were used. These two grid sizes are named "*Base*" and "*Fine*" for further simulations. Here, the normalized time step size of 0.02 was adopted. As observed, a change in both frequency and amplitude of the plate deformation is negligible. This approves the sufficiency of the *Base* grid for the analysis of this problem.

B. Freely vibrating low mass-ratio cylinder in a laminar flow

As the mass ratio decreases, the influence of added mass on the level of interaction between flow and structure rises causing a remarkable deviation of the response frequency from the Strouhal number.[44] Moreover, the numerical simulation encounters with challenging instabilities due to the effects of comparable added mass. In this part, a two-dimensional laminar flow at $Re = 150$ is simulated passing over a freely vibrating cylinder where the mass ratio, m^* is set as in Eq. (14)

$$m^* = 4m_s \Big/ \left(\rho_f \pi D^2\right) = 2. \tag{14}$$

Here, a unit length is considered for the depth of the domain, and a damping factor of $\zeta = 0.007$ is set. The cylinder is attached to a linear

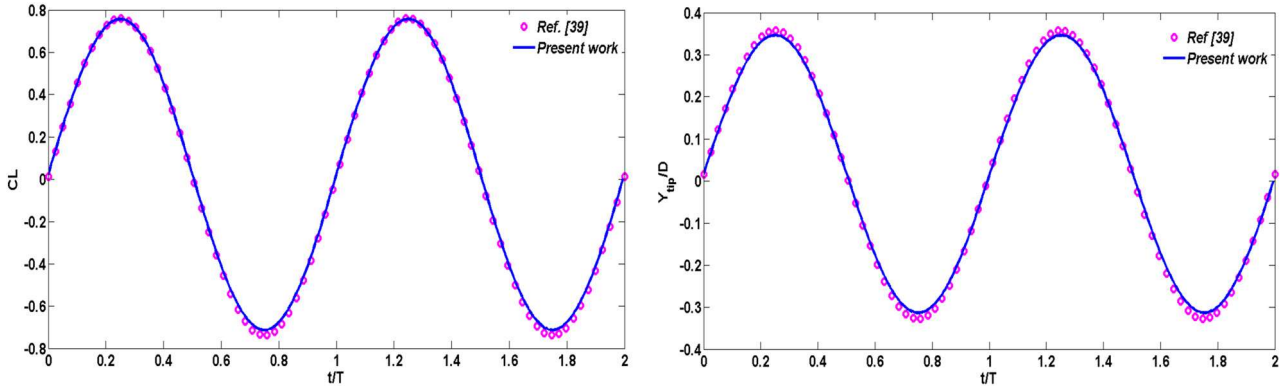

FIG. 3. Lift coefficient and tip displacement validation for the cylinder-splitter plate system.

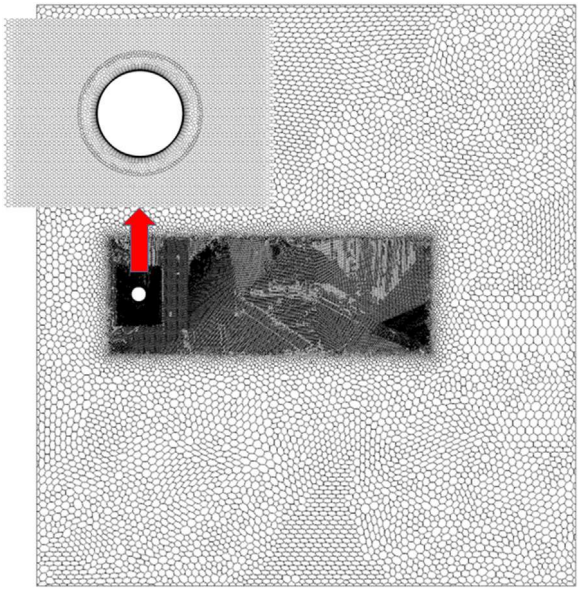

FIG. 4. Numerical domain and the grid refinement in the wake and the overset zones.

spring and damper in a free-stream rectangular domain whose boundary conditions are velocity inlet and pressure outlet. The cylinder surface is set as no-slip wall and its motion is handled by overset technique. To validate the results with literature,[45,46] the reduced velocity, $V_r = U/f_n D$ is changed over the range of $3 - 10$. The size of the domain is $36D \times 40D$. A base grid size of $0.5D$ was set for the domain while a zone with finer grid was adopted in the wake of the cylinder with size of $0.05D$. Furthermore, an overset region with a grid size of $0.03D$ was generated which provides a more robust handling of cylinder motion without any remeshing need. This region is demonstrated in a close picture mentioned by a red arrow. It is noteworthy that the motion of cylinder as well as the fixed end of the spring-damper system must be defined in appropriate coordinate systems to accurately calculate the spring-damper forces. Figure 4 illustrates the domain and grid topology used in this simulation.

Figure 5 depicts the maximum normalized amplitude of the cylinder response compared with Refs. 45 and 46. As it can be noted, the lock-in phase takes place in $4 < V_r < 7$ where the maximum response occurs which is interesting for the energy harvesting applications. It is also noticeable that the computational grids used for those two numerical references were quadrilateral whereas the polyhedral cells were adopted here which are known to be superior in terms of more accurate computation of gradients in highly vortical flows. Moreover, the grid motion applied in this work was the overset technique which maintained the original quality of the grid with high accurate linear interpolation between the background and the overset domains. However, diffusion-based morphing mesh motion was used in those two references where the shape and orthogonality of cells normally change during the simulation time. Nevertheless, satisfactory agreement in capturing different branches of the cylinder oscillatory response proves the adoption of proper numerical techniques including overset grid interpolation, spring-damper fixed reference locations, and reliable vortex

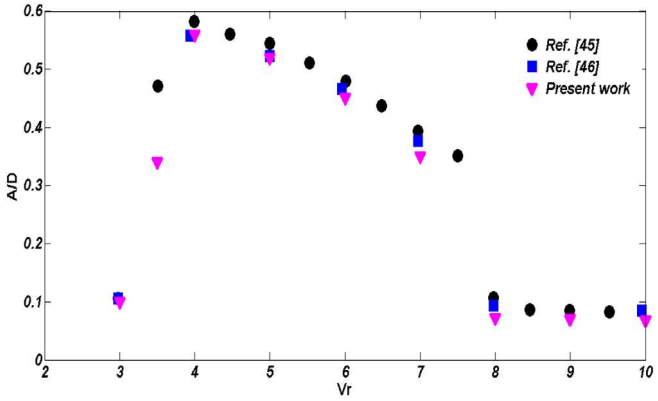

FIG. 5. Normalized amplitude of the vibrating cylinder at different reduced velocities.

shedding detection over and behind the oscillatory cylinder which are all employed for the main combined problem studied in Sec. IV.

In Fig. 6, the von Kármán vortex street is observed behind the induced-vibrating cylinder. Since the cylinder is oscillating in the transverse direction with remarkable velocity, the shed vortices have also a significant velocity component in transverse direction causing a wider distance between the core of vortices right after the cylinder which gradually get closer to each other due to the viscosity effects and energy dissipation in the downstream of the cylinder.

In the validation process, the reliability and accuracy of the FEM solver of STAR-CCM+ for precise handling of a hyperelastic plate and the morphing mesh solver was first examined. Due to low stiffness of the plate, it was difficult to numerically converge the deformation of the plate and also obtain physical outcome. Results of Fig. 3 and Table II ensured the authors that the flow field around the hyperelastic plate was properly captured and the solution data were grid-independent. Then, the results of Fig. 5 confirmed the reliability and validity of flow field interaction with the rigid motion of the spring-based cylinder using the overset mesh motion algorithm. Having validated all these relevant physics and the numerical techniques, the main problem, i.e., the flow interference between the upstream oscillating cylinder and the downstream hyperelastic plate is explored from energy harvesting point of view. In other words, it was crucial to first validate and ensure about the following technical steps before studying the main problem:

- Hyperelastic deformation of the piezoelectric splitter plate which depends on mesh morpher robustness, accurate flow field

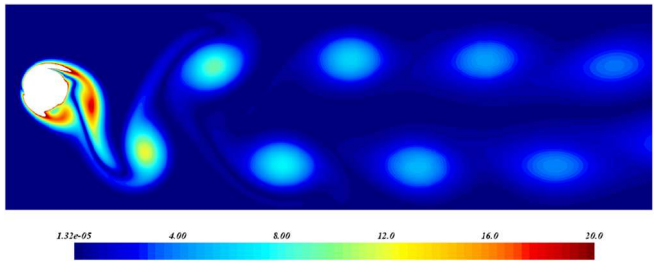

FIG. 6. Contour of normalized vorticity magnitude, $\omega_z D/U_{ref}$.

computation around the plate, the interface data interpolation, and time step size of integration.
- Interface data interpolation between the overset and background grids and second-order time integration of the vibrating cylinder equation of motion [Eq. (4)].

IV. COMBINED CONFIGURATION

Having presented the results of validation for two benchmark studies, the main problem consisting of a channel-confined oscillating one degree-of-freedom cylinder placed in the upstream of a fixed one to which a hyperelastic plate is attached, is further investigated and the influence of different concentric distances between the two cylinders ($x/D = 1.5, 2, 3, 4$) as well as the reduced velocity of the vibrating cylinder ($V_r = 3, 3.5, 4$) are investigated. Figure 7 illustrates a schematic of the problem.

The downstream cylinder and the attached splitter plate are at fixed location in the domain while the upstream cylinder is placed at four different distances from the downstream one. The Reynolds number is fixed at 200 based on the diameter of the cylinders, and the $m^*\zeta$ is set to 0.3 to reach the maximum extracted power.[8] It should be noted that in Ref. 8, different ratios of channel width to the cylinder diameter (H/D = 2, 2.5, 3, and 4) were studied, and the optimum $m^*\zeta$ was found to be in the range of 0.2–0.3 in terms of the maximum energy production. For H/D = 4 which is the ratio in this study, the maximum value of $m^*\zeta$ is 0.3. Therefore, this value was selected and fixed for this study.

The structure properties of the flexible plate are the same as in Table I. The geometrical properties of the splitter plate, the base grid size of fluid and solid domains, and the normalized time step size are all adopted based upon the findings from Sec. III A. The total number of cells in the solid and fluid domains were 450 and 75 000, respectively. At each time step, 40 iterations were considered so that all residuals reached 10^{-5} or below. A close view of the grid within the plate and fluid domains including the overset region is displayed in Fig. 8.

V. RESULTS AND DISCUSSION

In order to realize the influence of the combined system on the power efficiency, the response of the isolated oscillatory cylinder being placed between the parallel walls was computed first. Due to the presence of blockage effect of the channel walls, the vortex shedding from the oscillating cylinder, the vortical flow field in the wake and consequently the dynamic response of the cylinder are different from those of oscillating cylinder at far field which was studied as a validation

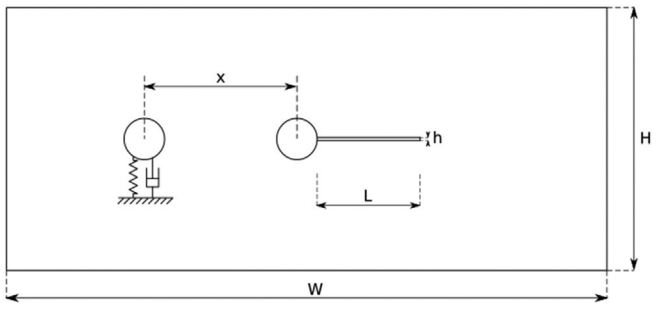

FIG. 7. A schematic of the combined configuration problem.

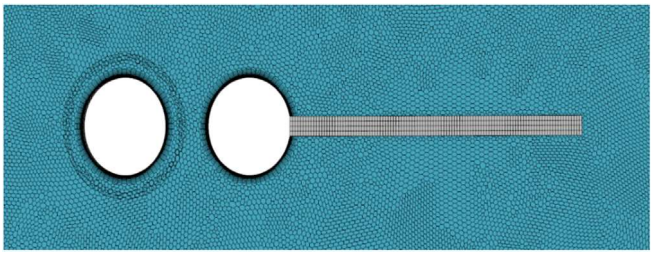

FIG. 8. Close view of the fluid, solid, and the overset grids.

problem in Sec. III B. As a result, the level of maximum power efficiency can rise up to an order of magnitude compared to the unconfined oscillation in far field for laminar flow.[8] Figure 9 shows the velocity contour of the flow field at various time instances corresponding to different cylinder location normalized with maximum velocity at each time instance. The left column represents the flow field during downward motion while the right one demonstrates the velocity field in the upward direction both following a sinusoidal trend. The formation of low velocity region close to the confined walls of the channel is clearly due to no-slip condition. As the cylinder approaches the lower wall, the distance between the cylinder and the channel wall decreases and thus the flow accelerates more at the lower surface of cylinder. In addition, the wake of cylinder is shifted to the upward direction by high local momentum over the lower surface. As can be observed in the first instance of the upward motion in right column, a remarkable high velocity region is shaped over both lower and upper surface of the cylinder. At this time instance, the velocity of cylinder is zero and the direction of the motion is being changed toward the upward direction.

Now, we present the results of the combined configuration. The power efficiency of the vibrating cylinder in the combined configuration, i.e., η_{com} computed according to Eq. (8) is expressed in Table III. At $V_r = 3$ for $x/D = 1.5$ and 2, no oscillation was experienced by the upstream cylinder and hence the amount of cylinder velocity was zero yielding in no power produced according to Eq. (6). This happened due to the absence of vortex shedding from the upstream cylinder as a result of relatively high spring stiffness for such a small spacing distance preventing from the shedding phenomenon over the upstream cylinder. However, the unsteady shedding takes place at higher distances. Moreover, it was found that at $V_r = 3.5$ and 4, the maximum efficiency value can be harvested at x/D=2. Based on the results, the highest expected efficiency was obtained at $x/D = 3$ and $V_r = 3$.

The power efficiency extracted by an isolated cylinder oscillating in the absence of cylinder-splitter plate in downstream, denoted by η_{iso} is shown in Table IV with maximum power efficiency at $V_r = 3$. As can be noticed, by increasing the reduced velocity, the efficiency remarkably drops due to getting farther from the lock-in condition. In order to make an assessment between the amount of maximum efficiency of combined configuration presented in Table III and the one given for the isolated cylinder, the second row of Table IV gives the relative change. Interestingly, results confirm a substantial rise in efficiency value of the oscillating cylinder while being placed in the upstream of this combined arrangement in comparison to the isolated configuration. This relative change is from 29.7% at $V_r = 3$% to 566% at $V_r = 4$ which approves by adding the second cylinder-splitter elastic plate in downstream, the presence of such vortical flow can

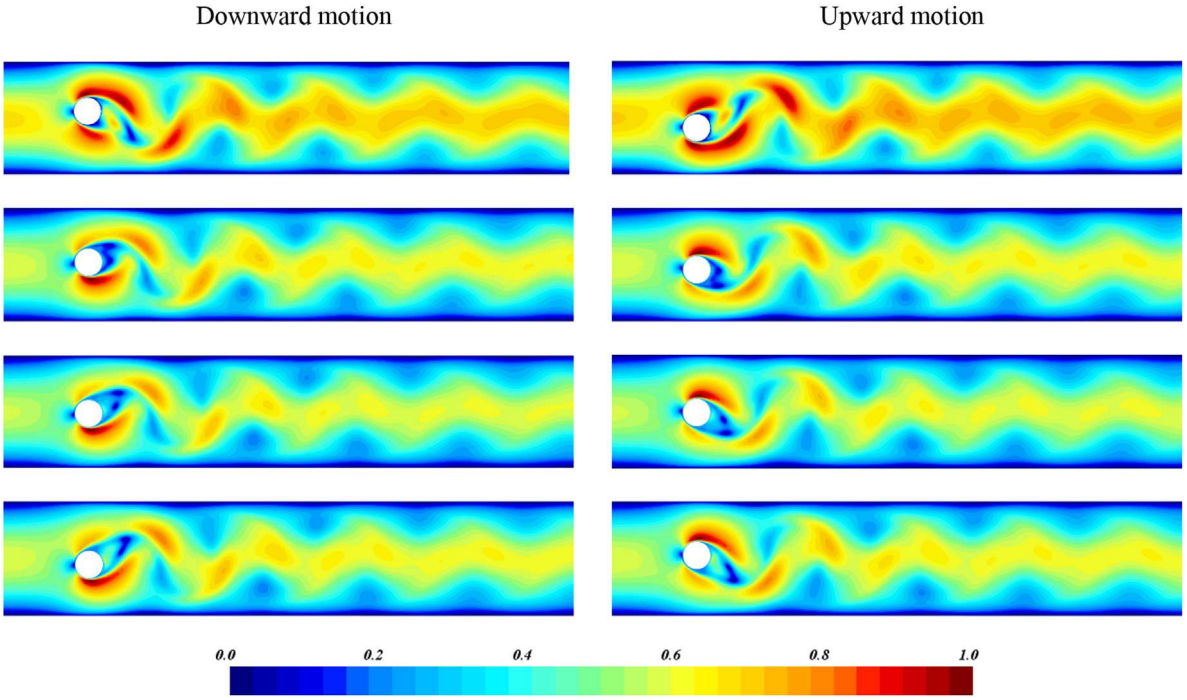

FIG. 9. Contour of the normalized velocity field for isolated vibrating cylinder, U/U_{max}.

TABLE III. Power efficiency of the oscillatory cylinder in the combined configuration.

	$V_r = 3$	$V_r = 3.5$	$V_r = 4$
$x/D = 1.5$	0	0.3009	0.2647
$x/D = 2$	0	0.4308	0.3017
$x/D = 3$	0.4521	0.3108	0.1962
$x/D = 4$	0.3461	0.1955	0.0778

significantly impact on the upstream flow pattern and consequently, improves the energy harvesting efficiency of flow-induced vibrating cylinder.

A comparison among lift coefficients, cylinder velocities, and power efficiencies of the combined system with those of the isolated oscillatory cylinder is plotted in Fig. 10. According to the results of Table III, the maximum efficiency condition at each reduced velocity is chosen for comparison with the isolated cylinder at the same reduced velocity. The time axis is normalized with the period of natural frequency corresponding to each reduced velocity. It is seen that at

TABLE IV. Relative increase in power efficiency of the oscillating cylinder.

	$V_r = 3$	$V_r = 3.5$	$V_r = 4$
Isolated cylinder	0.3486	0.1778	0.0453
$\frac{(\eta_{com,\,max} - \eta_{iso})}{\eta_{iso}} \times 100$	29.7	142.3	566

$V_r = 3$ for $x/D = 3$, lift and velocity of the isolated oscillatory cylinder are although less but still close to the combined system and therefore, the amount of power efficiency in the combined system is slightly higher than the isolated case, i.e., 29.7%. However, for $V_r = 3.5$ and 4, the difference becomes completely noticeable such that at $V_r = 4$ for $x/D = 2$, the value of power efficiency of the oscillatory cylinder for the combined system reaches almost 6.66 times of the one in isolated case.

In Table V, the normalized tip displacement of the hyperelastic plate in the combined arrangement is reported for different values of reduced velocities and spacing distances. In accordance with Table III, no vortex shedding and thus, no deformation is captured at $V_r = 3$ for $x/D = 1.5$ and 2. However, by increasing the distance between the cylinders, the response of the flexible plate becomes considerable. Though at higher reduced velocities, the shedding and plate deformation take place at the small spacing values as well. The highest amplitude of tip oscillation occurs at $x/D = 2$ for $V_r = 3.5$ and 4. Reminding the mean amplitude of an isolated cylinder-splitter plate system shown in Fig. 2, it is obvious that the combined system leads to larger deformations of the flexible plate which is favorable for the amount of power generated by a piezoelectric harvester based on Eq. (12).

A comparison between the highest normalized tip displacements of the splitter plate seen in Table V in the combined system with that of the isolated cylinder-plate case is depicted in Fig. 11. After the initial undeveloped flow field, a periodic behavior is observed in trends of all results with higher amplitude of tip oscillations for the combined system at $x/D = 2$ for $V_r = 3.5$ and 4 when the flow becomes fully developed.

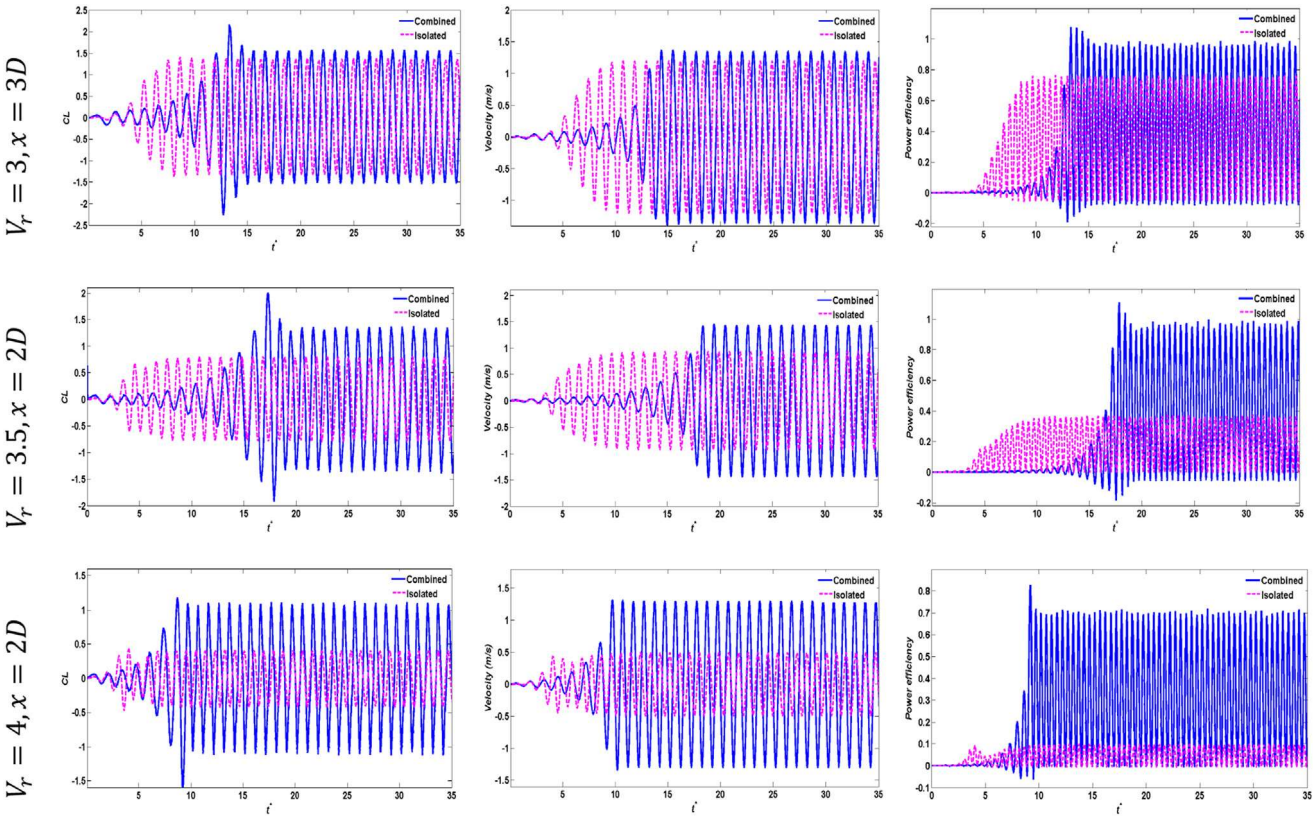

FIG. 10. The difference between VIV response of the confined isolated cylinder and the one in combined system.

TABLE V. Normalized tip displacement of the plate in the combined case.

	$V_r = 3$	$V_r = 3.5$	$V_r = 4$
$x/D = 1.5$	0	0.019 ± 0.391	0.006 ± 0.278
$x/D = 2$	0	0.026 ± 0.531	0.029 ± 0.507
$x/D = 3$	0.029 ± 0.357	0.026 ± 0.42	0.026 ± 0.448
$x/D = 4$	0.028 ± 0.357	0.03 ± 0.377	0.033 ± 0.378

The dominant frequency of the plate tip motion was computed for different spacing and reduced velocities using power spectral density of the displacement and is given in Table VII. The highest frequency is detected at $V_r = 3$ for $x/D = 3$ and 4. It is noteworthy that such thin elastic plates when subjected to fluid flow respond with a frequency on the order of their second mode in vacuum.[38] The natural frequencies of the under study elastic plate in vacuum were numerically computed using Eq. (11), and the first three values are 0.98, 6.18, and 17.31 Hz, respectively. Thus, it seems that for $V_r = 3$ and $x/D = 3$ and 4, the frequency of plate tip response is approching to the value of the second mode in vacuum. In other words, the value of $f_p/f_{n2} = \frac{6.15}{6.18} = 0.995$ for $V_r = 3$ and $x/D = 3$ which denotes the occurance of lock-in phenomenon for the plate tip displacement. Comparing the values of frequency in Table VI with that of isolated cylinder-splitter plate shown in Fig. 2 (5.28 Hz), one can conclude that at some spacing and reduced velocities, the response frequency is increased in contrast to some other circumstances.

According to Eq. (12), the ratio of the power generated by the piezoelectric harvester for all combined cases to that of the isolated cylinder-splitter plate, shown in Fig. 2, is computed and given in Table VII. In this table, the power ratio is computed by dividing the corresponding amplitude and third power of the frequency at each combined case by those of the isolated case, as follows:

$$\frac{P_{piezo,com}}{P_{piezo,iso}} = \frac{A_{com}}{A_{iso}} * \left(\frac{f_{com}}{f_{iso}}\right)^3. \tag{15}$$

As it is seen, a maximum rise of 67% is also obtained for the amount of power generated by the piezoelectric plate deformation at $V_r = 3$ and $x/D = 3$ in the combined system compared to the isolated cylinder-splitter plate. This increase arises from the stronger fluid–structure coupling caused by the presence of oscillatory cylinder in the upstream of the elastic plate.

In Fig. 12, the normalized tip displacement of plate and the corresponding power spectrum density of two combined cased are plotted and compared with the isolated splitter plate case studied at Sec. III A. The amplitudes of combined configuration at $V_r = 3$ for $x/D = 3$ and 4 are the same and a little higher than that of the isolated case, according to Table V, but due to the difference in the mean value, the minimum value of tip displacement is almost the same. The

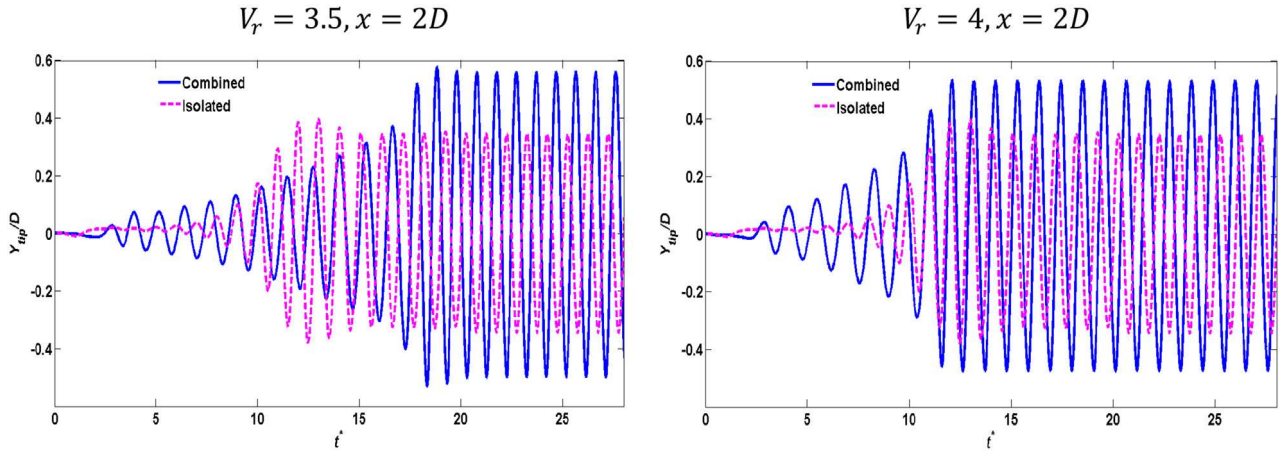

FIG. 11. Comparison of normalized tip displacement.

TABLE VI. Frequency of the tip displacement.

	$V_r = 3$	$V_r = 3.5$	$V_r = 4$
$x/D = 1.5$	0	4.07	3.62
$x/D = 2$	0	5.27	4.84
$x/D = 3$	6.15	5.64	5.37
$x/D = 4$	6.05	5.65	5.75

TABLE VII. Ratio of piezoelectric generated power, $P_{piezo,com}/P_{piezo,iso}$.

	$V_r = 3$	$V_r = 3.5$	$V_r = 4$
$x/D = 1.5$	0	0.53	0.26
$x/D = 2$	0	1.56	1.16
$x/D = 3$	1.67	1.52	1.39
$x/D = 4$	1.59	1.37	1.45

frequencies of the tip response for these two combined cases are also greater than that of the isolated cylinder-splitter plate, as given in Table VI.

In Fig. 13, normalized velocity contour of the flow field for different spacing and reduced velocity values are illustrated. All snapshots are corresponding to the time instance at which the plate tip deflection is maximum. As it is perceived, there is no vortex shedding and flow unsteadiness at $V_r = 3$ for the two smallest spacing values, i.e., $L/D = 1.5$ and 2. Under these circumstances, the wake of the upstream cylinder unifies with that of the second cylinder and since no asymmetric fluctuation takes place, the plate remains stationary leading to zero lift and power values by the whole system. However, by increasing the spacing distance between the two cylinders, the shedding phenomenon starts and the interaction between the vortices from the upstream and the downstream cylinders becomes remarkable and influential on the asymmetric flow field passing the flexible plate which yield in larger deflection of the piezoelectric energy harvester. Interestingly, as the spring stiffness and, consequently, the natural frequency of the upstream cylinder decrease, the oscillation of the cylinder excites its boundary layer making it separate. As a result, vortex shedding occurs

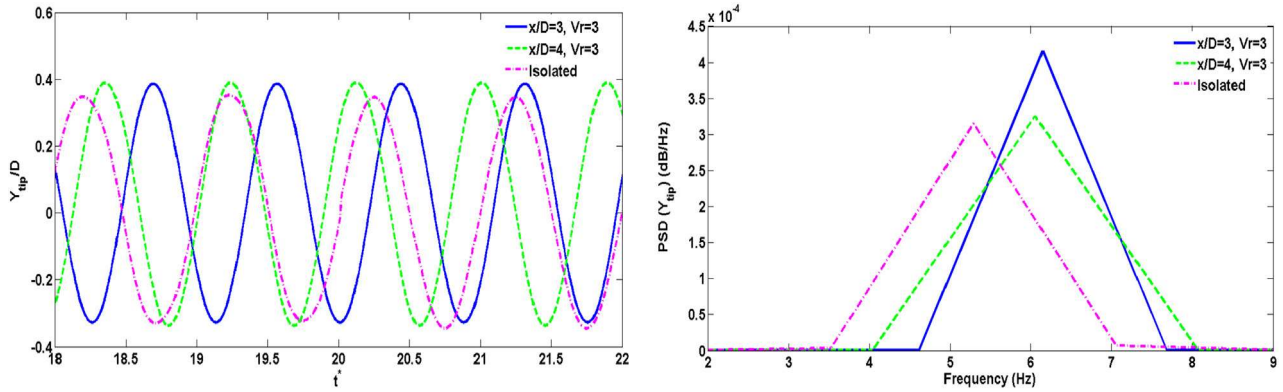

FIG. 12. Comparison of normalized plate tip response between combined and isolated cases.

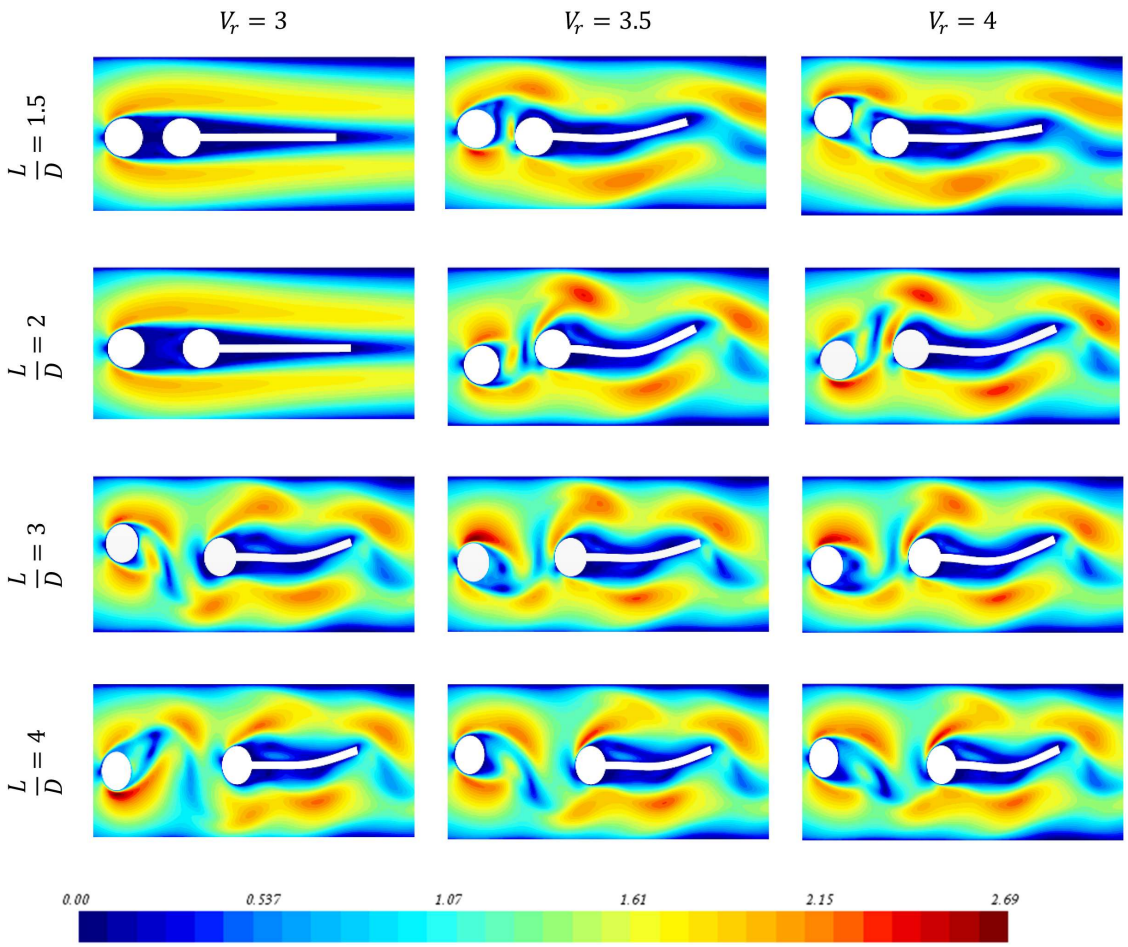

FIG. 13. Contour of the normalized velocity magnitude for the combined system, U/U_{ref}.

even at the two smallest spacing values for $V_r = 3.5$ and 4. It is also clear that the maximum tip deflection has happened at $L/D = 2$ and $V_r = 3.5$.

The results of sensitivity analysis of the numerical simulations for $L/D = 2$ and $V_r = 3.5$ are plotted in Fig. 14. The effect of two different normalized time step size is shown in Fig. 14(a). As observed, a small variation in the plate tip displacement confirms the independency of numerical outcomes from the adopted time step size in the simulations. Moreover, the influence of the grid size on the resolution of flow and structure fields was investigated and reported in Fig. 14(b). Two grid sizes named *Base* and *Fine* in Sec. III A were considered and negligible change in the plate tip displacement was achieved. This approves the sufficiency of the *Base* grid used for the parameters study reported in this section.

It is noteworthy that in order to more systematically identify the grid independence and uncertainty quantification, a robust well-studied validation and verification method proposed by ASME was exploited in an FSI modeling of a flat plate water entry.[47] However, three grid size and discretization levels are required for that method to compute some relevant parameters such as grid convergence index while only two grid sizes were tested in this work.

VI. SUMMARY AND CONCLUSION

In this paper, numerical study of a combined energy harvesting configuration was presented where a hyperelastic plate attached to a fixed cylinder was placed at the wake of an elastically mounted cylinder. Comparing to each isolated system, the vortical flow field was highly influenced by both the oscillating cylinder displacement as well as the elastic plate deformation. Three reduced velocities and four spacing values were studied to capture the effects on the flow field and consequently, the displacement amplitude and frequency of the oscillating cylinder and flexible plate. Based on the obtained results, no flow unsteadiness and vortex shedding was observed in the two smallest spacing values for $V_r = 3$. Though for higher spacing distances and reduced velocities, vortex shedding occurred, leading to larger displacement of cylinder and the piezoelectric plate. This improved the extracted power efficiency up to the maximum of five times for the isolated oscillating cylinder as well as a maximum power rise of about 56% and 60% generated by the piezoelectric plate by an increase in the tip displacement amplitude and frequency, respectively. Having ensured about the effectiveness of such combinations on the performance improvement in the context of energy harvesting, further

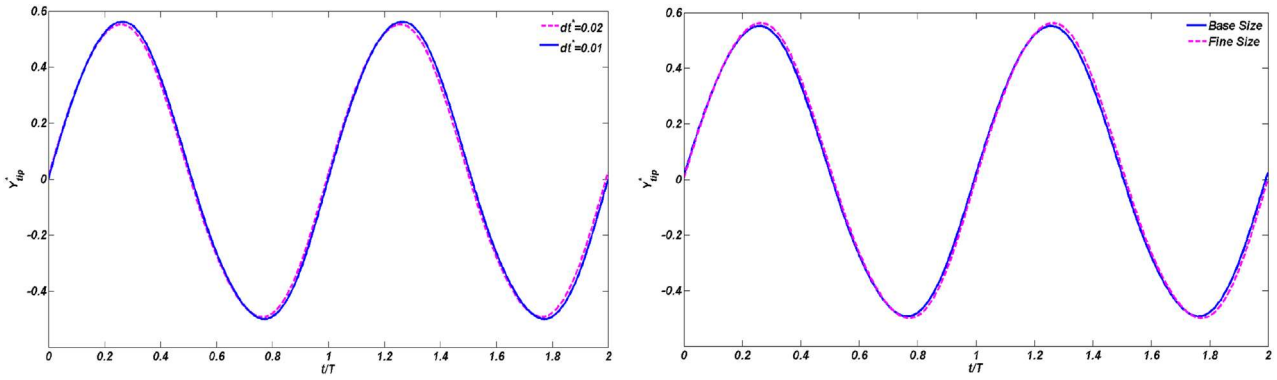

FIG. 14. Time-step and grid size study for the plate tip displacement (for $L/D = 2$ and $V_r = 3.5$).

analyses can be established about different elastic plate material properties, the effect of flow Reynolds number, the width of the channel and the shape of the bluff bodies for additional enhancements. Moreover, the method of fluid–solid momentum exchange[48] could be assessed for predicting the response of the hyperelastic plate in such confined low Reynolds flows in future studies. The flow field interference effect provided a great potential for energy extraction improvement from low speed flows in confined channels.

ACKNOWLEDGMENTS

This study was supported by the project IVANHOE (Installed adVAnced Nacelle uHbr Optimisation and Evaluation) within the European Union's Horizon 2020 research and innovation programme (Grant No. 863415) and the Strategic Research Project on Hydro- and Aerodynamic Initiative from Chalmers Foundation.

AUTHOR DECLARATIONS

Conflict of Interest

The authors have no conflicts to disclose.

Author Contributions

Massoud Tatar: Conceptualization (equal); Formal analysis (equal); Writing – original draft (equal); Writing – review & editing (equal). **Hua-Dong Yao:** Funding acquisition (equal); Resources (equal); Writing – review & editing (equal).

DATA AVAILABILITY

The data that support the findings of this study are available within the article.

REFERENCES

[1]H.-X. Zou, L.-C. Zhao, Q.-H. Gao, L. Zuo, F.-R. Liu, T. Tan *et al.*, "Mechanical modulations for enhancing energy harvesting: Principles, methods and applications," Appl. Energy **255**, 113871 (2019).
[2]J. Wang, L. Geng, L. Ding, H. Zhu, and D. Yurchenko, "The state-of-the-art review on energy harvesting from flow-induced vibrations," Appl. Energy **267**, 114902 (2020).
[3]C. H. Williamson and R. Govardhan, "Vortex-induced vibrations," Annu. Rev. Fluid Mech. **36**(1), 413–455 (2004).
[4]E. Taheri, M. Zhao, H. Wu, and A. Munir, "Energy harvesting from inline vibration of an elastically mounted circular cylinder in oscillatory flow," Ocean Eng. **239**, 109694 (2021).
[5]M. Zheng, D. Han, S. Gao, and J. Wang, "Numerical investigation of bluff body for vortex induced vibration energy harvesting," Ocean Eng. **213**, 107624 (2020).
[6]B. Lian, X. Tong, X. Zhu, Z. Du, Y. Cui, and B. C. Khoo, "Investigations on lock-in vortex-induced vibration of an airfoil at a high angle of attack based on detached eddy simulation," Phys. Fluids **35**(9), 094105 (2023).
[7]D. Brika and A. Laneville, "Vortex-induced vibrations of a long flexible circular cylinder," J. Fluid Mech. **250**, 481–508 (1993).
[8]A. K. Soti and A. De, "Vortex-induced vibrations of a confined circular cylinder for efficient flow power extraction," Phys. Fluids **32**(3), 033603 (2020).
[9]Y. Nakamura, K. Hirata, and T. Urabe, "Galloping of rectangular cylinders in the presence of a splitter plate," J. Fluids Struct. **5**(5), 521–549 (1991).
[10]J. Wang, S. Gu, C. Zhang, G. Hu, G. Chen, K. Yang *et al.*, "Hybrid wind energy scavenging by coupling vortex-induced vibrations and galloping," Energy Convers. Manage. **213**, 112835 (2020).
[11]G. Hu, K. T. Tse, M. Wei, R. Naseer, A. Abdelkefi, and K. Kwok, "Experimental investigation on the efficiency of circular cylinder-based wind energy harvester with different rod-shaped attachments," Appl. Energy **226**, 682–689 (2018).
[12]M. R. Mia, M. Zhao, and H. Wu, "Effects of heave motion of an elastically supported floating oscillating water column device on wave energy harvesting efficiency," Phys. Fluids **35**(1), 017115 (2023).
[13]M. Yu, X. Wang, J. Cai, V. Brazhenko, J. Tan, and Z. Xu, "Analysis on flow-induced vibration of square cylinders with different vibration forms and the flow energy harvesting capacity," Phys. Fluids **35**(9), 095124 (2023).
[14]M. Verma and A. De, "Dynamics of vortex-induced-vibrations of a slit-offset circular cylinder for energy harvesting at low Reynolds number," Phys. Fluids **34**(8), 083607 (2022).
[15]Y. Shen, J. Wang, H. Zheng, and Y. Sun, "Hydrodynamic energy collection using a cylinder with different cross sections based on macro-fiber composite," Phys. Fluids **35**(10), 102018 (2023).
[16]Y. Gu, D. Yurchenko, J. Wang, S. Li, S. Wei, and R. Tang, "Numerical analysis of reverse wake-induced vibration at low Reynolds number," Phys. Fluids **35**(7), 074116 (2023).
[17]N. Hosseini, M. Griffith, and J. Leontini, "The flow past large numbers of cylinders in tandem," J. Fluids Struct. **98**, 103103 (2020).
[18]T. Kitagawa and H. Ohta, "Numerical investigation on flow around circular cylinders in tandem arrangement at a subcritical Reynolds number," J. Fluids Struct. **24**(5), 680–699 (2008).
[19]T. Tsutsui, "Experimental study on the instantaneous fluid force acting on two circular cylinders closely arranged in tandem," J. Wind Eng. Ind. Aerodyn. **109**, 46–54 (2012).
[20]Z. Chen, M. M. Alam, B. Qin, and Y. Zhou, "Energy harvesting from and vibration response of different diameter cylinders," Appl. Energy **278**, 115737 (2020).

[21]R. Tang, Y. Gu, X. Mi, D. Yurchenko, F. Xu, W. Xu *et al.*, "Numerical analysis of WIV phenomenon with two in-series cylinders: WIV suppression and energy harvesting," Ocean Eng. **262**, 112154 (2022).
[22]L. Sanchez-de-Leon, F. Sastre, A. Barrero-Gil, and A. Velazquez, "Experimental study on energy harvesting maximization from the flow-induced vibration of a highly confined bluff body," Phys. Fluids **35**(8), 083106 (2023).
[23]H. D. Akaydin, N. Elvin, and Y. Andreopoulos, "Energy harvesting from highly unsteady fluid flows using piezoelectric materials," J. Intell. Mater. Syst. Struct. **21**(13), 1263–1278 (2010).
[24]M. Zhang and J. Wang, "Experimental study on piezoelectric energy harvesting from vortex-induced vibrations and wake-induced vibrations," J. Sens. **2016**, 2673292.
[25]J. Allen and A. Smits, "Energy harvesting eel," J. Fluids Struct. **15**(3–4), 629–640 (2001).
[26]J. Song, G. Hu, K. Tse, S. Li, and K. Kwok, "Performance of a circular cylinder piezoelectric wind energy harvester fitted with a splitter plate," Appl. Phys. Lett. **111**(22), 223903 (2017).
[27]X. Shan, R. Song, B. Liu, and T. Xie, "Novel energy harvesting: A macro fiber composite piezoelectric energy harvester in the water vortex," Ceram. Int. **41**, S763–S7 (2015).
[28]S. Orrego, K. Shoele, A. Ruas, K. Doran, B. Caggiano, R. Mittal *et al.*, "Harvesting ambient wind energy with an inverted piezoelectric flag," Appl. Energy **194**, 212–222 (2017).
[29]J.-X. Tao, B.-X. Zheng, X.-Y. Xu, T.-T. Tang, P. Yu, and C. Lu, "Numerical investigation on the coupled vibrations of piezoelectric energy harvester with a liquid-filled proof mass," Phys. Fluids **35**(6), 067103 (2023).
[30]H. Liu, S. Zhang, R. Kathiresan, T. Kobayashi, and C. Lee, "Development of piezoelectric microcantilever flow sensor with wind-driven energy harvesting capability," Appl. Phys. Lett. **100**(22), 223905 (2012).
[31]R. E. Cole and W. L. Neu, "Validation of a commercial fluid–structure interaction solver with applications to air cushion vehicle flexible seals," Ocean Eng. **189**, 106287 (2019).
[32]M. Sosnowski, J. Krzywanski, K. Grabowska, and R. Gnatowska, "Polyhedral meshing in numerical analysis of conjugate heat transfer," EPJ Web Conf. **180**, 02096 (2018).
[33]M. Tatar and M. H. Sabour, "Reduced-order modeling of dynamic stall using neuro-fuzzy inference system and orthogonal functions," Phys. Fluids **32**(4), 045101 (2020).
[34]D. Yan, T. Mikkola, P. Kujala, and S. Hirdaris, "Hydroelastic analysis of slamming induced impact on stiff and flexible structures by two-way CFD-FEA coupling," Ships Offshore Struct. **18**(9), 1300–1312 (2023).
[35]S. Alben, "Flag flutter in inviscid channel flow," Phys. Fluids **27**(3), 033603 (2015).
[36]D. T. Akcabay and Y. L. Young, "Hydroelastic response and energy harvesting potential of flexible piezoelectric beams in viscous flow," Phys. Fluids **24**(5), 054106 (2012).
[37]J. Liu, R. K. Jaiman, and P. S. Gurugubelli, "A stable second-order scheme for fluid–structure interaction with strong added-mass effects," J. Comput. Phys. **270**, 687–710 (2014).
[38]A. Kundu, A. K. Soti, R. Bhardwaj, and M. C. Thompson, "The response of an elastic splitter plate attached to a cylinder to laminar pulsatile flow," J. Fluids Struct. **68**, 423–443 (2017).
[39]S. Turek and J. Hron, "Proposal for numerical benchmarking of fluid-structure interaction between an elastic object and laminar incompressible flow," in *Fluid-Structure Interaction* (Springer, 2006), pp. 371–385.
[40]R. Bhardwaj and R. Mittal, "Benchmarking a coupled immersed-boundary-finite-element solver for large-scale flow-induced deformation," AIAA J. **50**(7), 1638–1642 (2012).
[41]J. Lee and D. You, "Study of vortex-shedding-induced vibration of a flexible splitter plate behind a cylinder," Phys. Fluids **25**(11), 110811 (2013).
[42]H. Wang, Q. Zhai, and J. Zhang, "Numerical study of flow-induced vibration of a flexible plate behind a circular cylinder," Ocean Eng. **163**, 419–430 (2018).
[43]M. Tatar and M. Masdari, "Investigation of pitch damping derivatives for the Standard Dynamic Model at high angles of attack using neural network," Aerosp. Sci. Technol. **92**, 685–695 (2019).
[44]X. Li, Z. Lyu, J. Kou, and W. Zhang, "Mode competition in galloping of a square cylinder at low Reynolds number," J. Fluid Mech. **867**, 516–555 (2019).
[45]B. Carmo, S. Sherwin, P. Bearman, and R. Willden, "Flow-induced vibration of a circular cylinder subjected to wake interference at low Reynolds number," J. Fluids Struct. **27**(4), 503–522 (2011).
[46]A. Viré, A. Derksen, M. Folkersma, and K. Sarwar, "Two-dimensional numerical simulations of vortex-induced vibrations for a cylinder in conditions representative of wind turbine towers," Wind Energy Sci. **5**(2), 793–806 (2020).
[47]D. Yan, T. Mikkola, A. Lakshmynarayanana, S. Tödter, T. E. Schellin, J. Neugebauer *et al.*, "A study into the FSI modelling of flat plate water entry and related uncertainties," Mar. Struct. **86**, 103296 (2022).
[48]S. Tavakoli, T. Mikkola, and S. Hirdaris, "A fluid–solid momentum exchange method for the prediction of hydroelastic responses of flexible water entry problems," J. Fluid Mech. **965**, A19 (2023).